

# 1 minute parity lifetime of a NbTiN Cooper-pair transistor

David J. van Woerkom,<sup>\*</sup> Attila Geresdi<sup>\*,†</sup> and Leo P. Kouwenhoven

*QuTech and Kavli Institute of Nanoscience, Delft University of Technology, 2600 GA Delft, The Netherlands.*

The parity modulation of the ground state of a superconducting island is a direct consequence of the presence of the Cooper pair condensate preferring an even number of charge carriers [1, 2]. The addition energy of an odd, unpaired quasiparticle equals to the superconducting gap,  $\Delta$ , suppressing single electron hopping in the low temperature limit,  $k_B T \ll \Delta$ . Controlling the quasiparticle occupation is of fundamental importance for superconducting qubits as single electron tunneling results in decoherence [3, 4]. In particular, topological quantum computation relies on the parity control and readout of Majorana bound states [5, 6]. Here we present parity modulation for the first time of a niobium titanite nitride (NbTiN) Cooper-pair transistor coupled to aluminium (Al) leads. We show that this circuit is compatible with the magnetic field requirement  $B \sim 100$  mT of inducing topological superconductivity in spin-orbit coupled nanowires [7–9]. Our observed parity lifetime exceeding 1 minute is several orders of magnitude higher than the required gate time of flux-controlled braiding of Majorana states [10]. Our findings readily demonstrate that a NbTiN island can be parity-controlled and therefore provides a good platform for superconducting coherent circuits operating in a magnetic field.

Experimentally, the parity modulation of a superconducting island can be observed via the ground state charge [2], the even-odd modulation of the charge stability diagram [11, 12], or the parity dependence of the switching current,  $I_{sw}$  [13]. The interplay of the charging energy  $E_c = e^2/2C$  and the Josephson coupling  $E_J = I_c \hbar/2e$  makes the Cooper-pair transistor (CPT) a single, gate-modulated Josephson junction [13, 14] with a  $2e$  charge periodicity in the absence of parity switches, i.e. infinitely long parity lifetime,  $\tau_p$ .

Recent, direct measurements of  $\tau_p$  [4, 15] yielded values up to the millisecond regime for aluminium devices. Despite considerable efforts, however, no  $2e$  periodicity has been reported for non-aluminium superconductors [16–18], such as niobium or vanadium. Comparative studies of aluminium and niobium CPTs suggested that the elusiveness of parity effects is related to the mate-

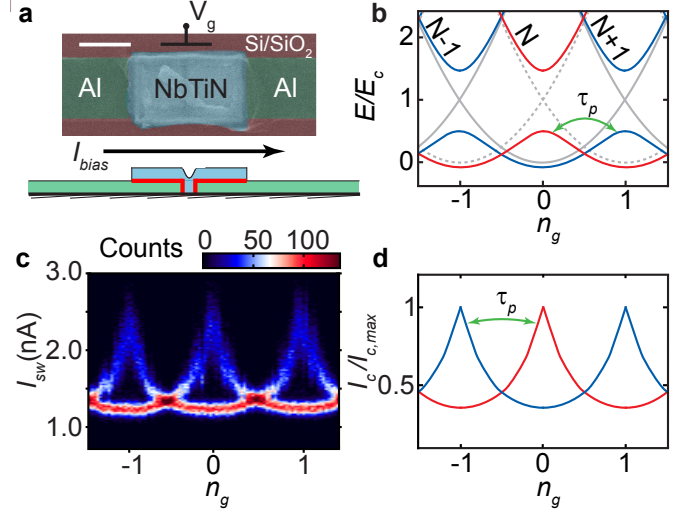


FIG. 1. **Device layout and parity-dependent switching current.** (a) Scanning electron microscope image and schematic cross-section of a typical Al/NbTiN/Al hybrid Cooper-pair transistor (CPT). The NbTiN island dimensions are  $250 \text{ nm} \times 450 \text{ nm}$ . Scale bar denotes  $200 \text{ nm}$ . The  $\text{AlO}_x$  oxide barriers are indicated by thick red lines. (b) Energy level diagram as a function of the gate charge,  $n_g$ , in the presence of low energy subgap states restoring  $1e$  periodicity. Gray lines denote energy levels in the absence of Josephson coupling, i.e.  $E_J = 0$ . Red and blue lines show energy levels for even and odd charge parity respectively, both for  $E_J = E_c$ . Parity switches occur on the timescale of  $\tau_p$  due to quasiparticle tunneling. Measured switching current histogram (c) and calculated  $I_c(n_g)$  (d) in the low temperature limit. Note that in (d) the two possible  $I_c(n_g)$  values corresponding to the even and odd charge states denoted by blue and red lines respectively. In the measured data (c) the two branches are superimposed, see text.

rial properties [17], in accordance with earlier measurements showing that subgap quasiparticle states may appear in niobium due to oxidation of the bulk material [19]. In contrast, nitridized niobium compounds, such as niobium titanite nitride (NbTiN), have been shown to be less prone to form oxides and hence are good candidates for parity-conserving superconducting circuits. Furthermore, NbTiN forms transparent contacts with spin-orbit coupled semiconductor nanowires [9], and has become a preferred superconductor to investigate Majorana bound states.

Our device features a NbTiN island sputtered onto Al leads (Fig. 1a). The tunnel barriers between the island and the leads are created by means of controlled *in-situ* surface oxidation of Al, resulting in amorphous  $\text{AlO}_x$

<sup>\*</sup> These authors contributed equally to this work.

<sup>†</sup> Corresponding author, e-mail address: a.geresdi@tudelft.nl

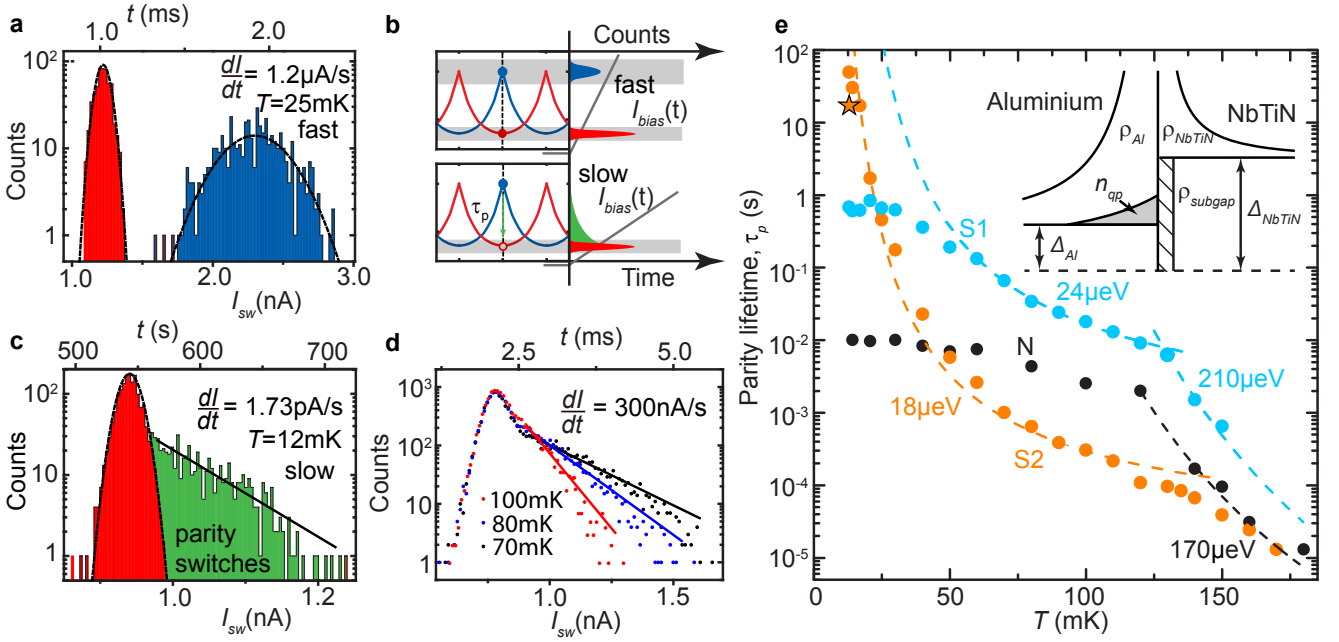


FIG. 2. **Characterization and temperature dependence of the parity lifetime.** (a) Linecut histogram at integer  $n_g$  of Fig. 1c showing a bimodal distribution. We attribute the two peaks to the two parity states of the CPT (colored red and blue, respectively). (b) For a *fast* current ramp (upper panel), the histograms of the two parity states are independently probed showing the characteristics of data in panel (a). In the *slow* limit (lower panel in (b)), parity switches occur during the current ramp, leading to an exponential tail of the distribution (shown in green), quantifying  $\tau_p$ . The  $I_{\text{bias}}(t)$  current ramp is represented by a dark gray line. (c) Experimental dataset in the *slow* limit. Note the change in the current- and timescale compared to panel (a). We show the exponential cutoff in green, and extract  $\tau_p = 49$  s (solid black line). (d) Experimental data at different temperatures show the temperature dependence of  $\tau_p$ . (e)  $\tau_p$  as a function of temperature for non-shielded device N, and shielded devices S1, S2. For detailed comparison, see the main text and the supplementary material. All CPTs exhibit an activated behavior with  $\Delta \approx 170 \dots 210 \mu\text{V}$  in the high temperature limit corresponding to the gap of the aluminium leads. Saturation of device N without shielding and no quasiparticle traps is observed below  $T \approx 100$  mK. Shielded devices S1 and S2 exhibit a minigap-activated behavior  $\Delta^* \approx 20 \mu\text{V}$  in the low temperature limit. The fitted  $\tau_p(T)$  function is defined in the main text. Star symbol shows  $\tau_p = 15$  s at  $T = 12$  mK extracted from parity distilled data for device S2 (see Fig. 3d).

barriers [20].

We extract a charging energy  $E_c \approx 50 \mu\text{eV}$  from the measured charge stability diagram. For different devices, we estimate  $E_J \approx 30 \dots 50 \mu\text{eV}$  from the superconducting gaps and normal state resistances of the junctions [21] assuming equal resistances for the two tunnel barriers. A detailed list of parameters and characterization methods are presented in the supplementary material. Our devices are in the intermediate coupling regime with  $E_J \sim E_c$ , where the energy diagram (Fig. 1b) and the critical current (Fig. 1d) are sensitive to the charge parity. It is important to note that our CPTs are in the optimal regime to establish flux-controlled braiding of Majorana bound states with  $E_J \sim E_c \gg k_B T$  [10] and hence a useful platform to establish the parity lifetime for Majorana circuits [22].

We model the CPT as a two level system which can exist in either parity state (red and blue bands in Fig. 1, respectively), and switches state on the timescale of  $\tau_p$  [23] due to quasiparticle tunneling. We collect the switching current histograms by repetitively sweeping the bias

current from zero (non-dissipative state) to beyond the switching current. Here, in the resistive state, quasiparticle tunneling causes a random reinitialization of the parity state of the CPT for the next measurement. This results in the apparent  $1e$  periodicity in Fig. 1c. Nevertheless, as long as the parity remains constant during each sweep, we expect to find the two branches as a bimodal histogram, as we indeed observe in Fig. 2a. In these measurements, the current ramp time is much shorter than the parity lifetime,  $\tau_p$  (*fast* measurement limit).

We quantify  $\tau_p$  in the *slow* measurement limit. In this regime parity switches occur during the current ramp (Fig. 2b lower panels) such that reaching the upper branch (depicted as blue in Fig. 2a and 2b) becomes exponentially suppressed (Fig. 2c). The exponential tail represents parity switches during the current bias ramp, resulting in an observable decay of the upper branch (depicted as green in Fig. 2b and 2c),  $p_u(t) = p_u(0) \exp(-t/\tau_p)$ . Thus, from the decay of the histogram (black solid line in Fig. 2c), we can directly obtain  $\tau_p$ .

The observed  $\tau_p$  is a result of single electron tunneling events through the junctions of the CPT. In the zero voltage state, we can link  $\tau_p$  to the subgap density of states on the island and the quasiparticle density in the leads [24] (for details see the supplementary material):

$$\tau_p^{-1} = \frac{2n_{\text{qp}}}{e^2 R_N \rho_{\text{Al}}} \frac{\rho_{\text{subgap}}}{\rho_{\text{NbTiN}}}, \quad (1)$$

where  $R_N$  is the normal state resistance of the CPT. It is instructive to note that the parity lifetime is determined by the quasiparticle density in the leads [22] and the *phenomenological* Dynes parameter [25] of the island material. Assuming a thermal  $n_{\text{qp}}(T) \propto \sqrt{T} \exp(-\Delta_{\text{Al}}/k_B T)$  in the leads, we find  $\Delta_{\text{Al}} = 170 \dots 210 \mu\text{eV}$  (Fig. 2e) for temperatures exceeding 120 mK, in good agreement with the superconducting gap of the aluminium leads extracted from the charge stability diagram. We can therefore attribute the observed parity lifetime for  $T > 120 \text{ mK}$  to the *thermal* quasiparticle population in the leads.

For device N, however, we find a saturated  $\tau_p = 9.5 \text{ ms}$  in the low temperature limit, a common observation in superconducting qubits [4] and hybrid single electron transistors [24] signifying the presence of *non-thermal* quasiparticle excitations.

We further improve the low temperature parity lifetime by introducing microwave-tight shielding coated with infrared absorber painting and Ti/Au quasiparticle traps for devices S1 and S2. These additions result in a non-saturated behaviour of  $\tau_p$ , and we observe a minigap activated behaviour with  $\Delta^* \approx 20 \mu\text{eV}$  for both devices. It is to be stressed that this observation signals that the effective quasiparticle temperature of the CPT follows the bath temperature down to the 10 mK regime. We find  $\tau_p = 49 \text{ s}$  at  $T = 12 \text{ mK}$  for device S2. To put this number into context, we note that the Josephson frequency  $f_J = E_J/h \approx 10 \text{ GHz}$  and thus a single quasiparticle event occurs only once for every  $\tau_p f_J \sim 10^{11}$  Cooper pairs tunneling through the junctions. This signifies the low probability of parity switches for an open device with  $E_J \approx E_c$  required for flux-tunable Majorana braiding schemes.

Thus far, we started each switching current measurement from an unknown parity state because of the random reinitialization in the dissipative state of the CPT for  $I_{\text{bias}} > I_{\text{sw}}$ . In order to reproducibly select the same parity state, we employ a parity distillation protocol (Fig. 3) where, by selecting a single parity state without switching to the resistive state, we ensure that the parity remains well defined for the subsequent measurement. This protocol indeed results in a  $2e$  periodic switching current pattern (Fig. 3c) which is observed for the first time for a non-aluminium CPT.

We quantify the effectiveness of the parity distillation

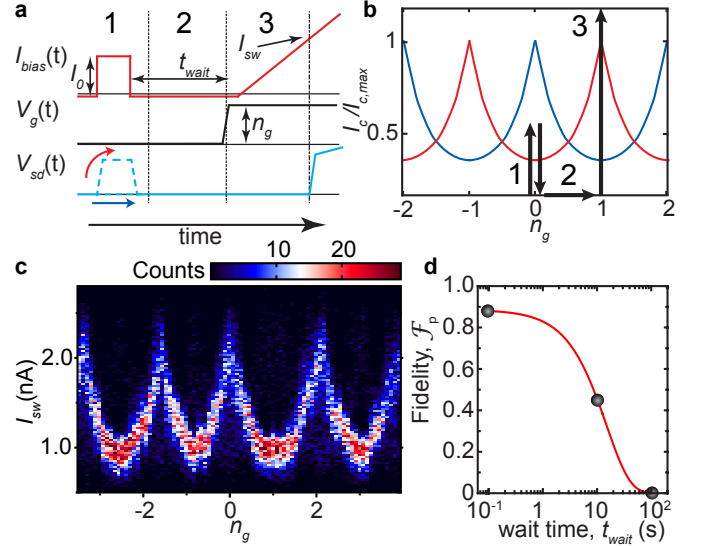


**FIG. 3. Parity state distillation.** (a) Schematic current bias and gate voltage waveforms applied to the device. First, current bias pulse with an amplitude between the two branches is applied (1). At the same time the measured voltage  $V_{\text{sd}}(t)$  is recorded to initialize the parity state. Then the gate voltage is ramped (2) and finally, the switching current is recorded (3). (b) The schematic representation of the applied waveforms overlaid on the parity-dependent critical current. (c) Parity distilled switching current histogram exhibiting  $2e$  periodicity with  $t_{\text{wait}} = 100 \text{ ms}$ . (d) Parity distillation fidelity as a function of  $t_{\text{wait}}$ , see main text. Solid red line denotes the fit  $\sim \exp(-t_{\text{wait}}/\tau_p)$  with  $\tau_p = 15 \text{ s}$ . All data was recorded on device S2.

by defining the fidelity as:

$$\mathcal{F}_p = \frac{p_{u,f} - p_{u,i}}{1 - p_{u,i}}, \quad (2)$$

where  $p_{u,f}$  is the conditional probability of the upper branch in the final step (3), and  $p_{u,i}$  is the initial probability. We note that the above expression is valid for an arbitrary  $0 < p_{u,i} < 1$  value set by the average quasiparticle occupation of the CPT. For device S2 we find  $\mathcal{F}_p = 0.88 \pm 0.05$  for  $t_{\text{wait}} = 100 \text{ ms}$  demonstrating the high degree of parity distillation. By changing  $t_{\text{wait}}$  between the parity initialization (1) and measurement (3), we acquire an independent measurement  $\tau_p = 15 \text{ s}$  for device S2 at  $T = 12 \text{ mK}$  (Fig. 3d).

Finally, we investigate the evolution of  $\tau_p(B)$  in different magnetic field directions. In parallel magnetic field, we observe a gradual decrease of  $\tau_p$ . The onset of the steep decay at  $B = 110 \text{ mT}$  (yellow arrow in Fig. 4a) is in agreement with the condition for vortex penetration through a mesoscopic superconducting island [26] with  $\Phi \approx 1.1\Phi_0 \gtrsim \Phi_0$ . This result underlines the significance of the sample geometry for magnetic field-enabled CPTs to avoid vortex formation. However, our device exhibits  $\tau_p > 10 \text{ ms}$  in  $B_{\parallel} > 100 \text{ mT}$ , required to induce Majorana

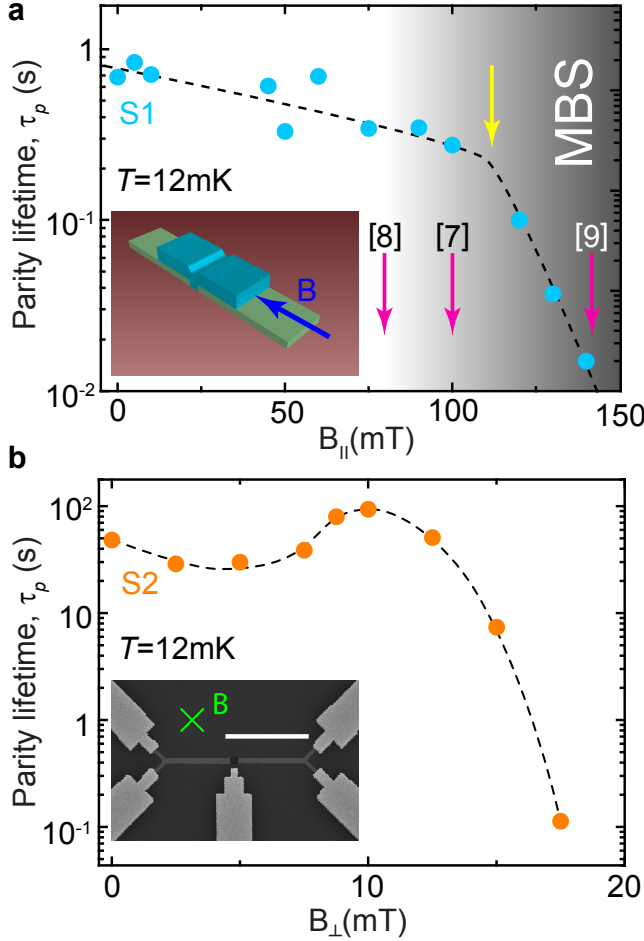


FIG. 4. **Influence of the magnetic field on the CPT.** (a) The parity lifetime as a function of the in-plane field,  $B_{||}$  pointing as shown in the inset. The shaded region depicts the condition for inducing Majorana bound states (MBS) in spin-orbit coupled semiconductor wires [7–9]. The change in slope at  $B \approx 110$  mT is denoted by the yellow arrow and the dash line serves as a guide to the eye. (b) The parity lifetime as a function of perpendicular field,  $B_{\perp}$ . The dash line shows the overall trend. The inset shows the electron microscope image of the device with the white scale bar denoting  $5 \mu\text{m}$ .

bound states [7–9].

In contrast, applying a perpendicular field first results in an increase of  $\tau_p$  reaching a maximum value  $\tau_p = 94$  s at  $B_{\perp} \approx 10$  mT, before dropping at higher magnetic fields (Fig. 4b). Making use of the relation between the lower critical field and the stripe width,  $B_{c1}(w) \sim \Phi_0/w^2$  [27] we attribute the initial increase to vortex formation and hence more effective quasiparticle trapping in the wide lead sections ( $w \approx 2 \mu\text{m}$ ) of the device (see wide light gray sections in Fig. 4b). Upon reaching  $B \approx 10$  mT, the vortex phase becomes stable in the close vicinity of the CPT ( $w \approx 250$  nm) causing a gradual decrease of  $\tau_p$ . We note that due to  $\xi_{Al} \approx 100$  nm  $\sim w$  for our devices, we cannot make a quantitative comparison between our

measurement data and theoretical expressions of critical magnetic field of thin stripes. We however conclude that vortices induced by a perpendicular magnetic field can increase the efficiency of quasiparticle traps, but the formation of a vortex phase in the near vicinity of the CPT enhances quasiparticle transport in agreement with earlier observations [28, 29].

In conclusion, we fabricated and characterized NbTiN Cooper-pair transistors showing parity effects for a non-aluminium superconductor for the first time. We characterize the parity lifetime by evaluating the switching current histograms and find values exceeding 1 minute at  $T = 12$  mK. Our devices are in the regime of  $E_j \sim E_c \gg k_B T$  ideal for Majorana braiding schemes. Furthermore, we demonstrate charge parity distillation to reproducibly initialize the island in a given parity state. We find parity lifetimes in excess of 10 ms in external magnetic fields up to 150 mT and showed the importance of sample geometry for magnetic field-enabled operation required for inducing Majorana bound states.

The authors thank A. R. Akhmerov, S. Rubbert, Y. Nazarov, R. Lutchyn and J. Pekola for fruitful discussions and R. N. Schouten for technical assistance. This work has been supported by the Netherlands Foundation for Fundamental Research on Matter (FOM) and Microsoft Corporation Station Q. A. G. acknowledges funding from the Netherlands Organisation for Scientific Research (NWO) through a VENI grant.

D. J. W. fabricated the devices. D. J. W. and A. G. performed the measurements. D. J. W., A. G. and L. P. K. discussed the data, contributed to the analysis and wrote the manuscript.

- 
- [1] D. Averin and Y. Nazarov, Phys. Rev. Lett. **69**, 1993 (1992).
  - [2] P. Lafarge, P. Joyez, D. Esteve, C. Urbina, and M. H. Devoret, Nature **365**, 422 (1993).
  - [3] J. Clarke and F. K. Wilhelm, Nature **453**, 1031 (2008).
  - [4] D. Riste, C. C. Bultink, M. J. Tiggelman, R. N. Schouten, K. W. Lehnert, and L. DiCarlo, Nat Commun **4**, 1913 (2013).
  - [5] J. Alicea, Reports on Progress in Physics **75**, 076501 (2012).
  - [6] N. Read, Phys. Today **65**, 38 (2012).
  - [7] R. M. Lutchyn, J. D. Sau, and S. Das Sarma, Phys. Rev. Lett. **105**, 077001 (2010).
  - [8] Y. Oreg, G. Refael, and F. von Oppen, Phys. Rev. Lett. **105**, 177002 (2010).
  - [9] V. Mourik, K. Zuo, S. M. Frolov, S. R. Plissard, E. P. A. M. Bakkers, and L. P. Kouwenhoven, Science **336**, 1003 (2012).
  - [10] T. Hyart, B. van Heck, I. C. Fulga, M. Burrello, A. R. Akhmerov, and C. W. J. Beenakker, Phys. Rev. B **88**, 035121 (2013).
  - [11] M. T. Tuominen, J. M. Hergenrother, T. S. Tighe, and M. Tinkham, Phys. Rev. Lett. **69**, 1997 (1992).

- [12] T. Eiles, J. Martinis, and M. Devoret, Phys. Rev. Lett. **70**, 1862 (1993).
- [13] P. Joyez, P. Lafarge, A. Filipe, D. Esteve, and M. H. Devoret, Phys. Rev. Lett. **72**, 2458 (1994).
- [14] L. J. Geerligs, V. F. Anderegg, J. Romijn, and J. E. Mooij, Phys. Rev. Lett. **65**, 377 (1990).
- [15] M. D. Shaw, R. M. Lutchyn, P. Delsing, and P. M. Echternach, Phys. Rev. B **78**, 024503 (2008).
- [16] R. Dolata, H. Scherer, A. B. Zorin, and J. Niemeyer, Journal of Applied Physics **97**, 054501 (2005).
- [17] A. M. Savin, M. Meschke, J. P. Pekola, Y. A. Pashkin, T. F. Li, H. Im, and J. S. Tsai, Applied Physics Letters **91**, 063512 (2007).
- [18] J. J. Toppari, T. Kühn, A. P. Halvari, J. Kinnunen, M. Leskinen, and G. S. Paraoanu, Phys. Rev. B **76**, 172505 (2007).
- [19] J. Halbritter, Applied Physics A **43**, 1 (1987).
- [20] W. D. Oliver and P. B. Welander, MRS Bulletin **38**, 816 (2013).
- [21] V. Ambegaokar and A. Baratoff, Phys. Rev. Lett. **10**, 486 (1963).
- [22] D. Rainis and D. Loss, Phys. Rev. B **85**, 174533 (2012).
- [23] R. M. Lutchyn, L. I. Glazman, and A. I. Larkin, Phys. Rev. B **74**, 064515 (2006).
- [24] O.-P. Saira, A. Kemppinen, V. F. Maisi, and J. P. Pekola, Phys. Rev. B **85**, 012504 (2012).
- [25] R. Dynes, V. Narayanamurti, and J. Garno, Phys. Rev. Lett. **41**, 1509 (1978).
- [26] V. V. Moshchalkov, L. Gielen, C. Strunk, R. Jonckheere, X. Qiu, C. V. Haesendonck, and Y. Bruynseraede, Nature **373**, 319 (1995).
- [27] G. Stan, S. B. Field, and J. M. Martinis, Phys. Rev. Lett. **92**, 097003 (2004).
- [28] J. T. Peltonen, J. T. Muhonen, M. Meschke, N. B. Kopnin, and J. P. Pekola, Phys. Rev. B **84**, 220502 (2011).
- [29] C. Wang, Y. Y. Gao, I. M. Pop, U. Vool, C. Axline, T. Brecht, R. W. Heeres, L. Frunzio, M. H. Devoret, G. Catelani, L. I. Glazman, and R. J. Schoelkopf, Nat Commun **5**, 5836 (2014).



# Supplementary online material

## 1 minute parity lifetime of a NbTiN Cooper-pair box

### DEVICE FABRICATION

The Cooper-pair transistors (CPTs) were fabricated using electron beam lithography and thin film deposition starting with a  $p^{++}$  doped silicon wafer with a 285 nm thick thermally grown  $\text{SiO}_2$  surface layer. First, aluminium leads were defined and evaporated in a high-vacuum chamber ( $p_{\text{base}} \sim 10^{-7}$  Torr) at a rate of 0.2 nm/s with a thickness of 30...35 nm. Subsequently, the mask for the NbTiN island was defined in a second lithography step. The sample was loaded into an ultra high vacuum AJA International ATC 1800 sputtering system ( $p_{\text{base}} \sim 10^{-9}$  Torr), where first a  $\sim 5$  nm Al layer was removed by means of argon plasma etching at  $p = 3$  mTorr. This step was followed by *in-situ* oxidation to create  $\text{AlO}_x$  tunnel barriers. Without breaking vacuum, the NbTiN island was then sputtered with a layer thickness of 70...100 nm.

We used a  $\text{Nb}_{0.7}\text{Ti}_{0.3}$  target with a diameter of 3". Reactive sputtering resulting in nitridized NbTiN films was performed in an Ar/N process gas with a typical 10 at% nitrogen content at a pressure of 3 mTorr using a DC magnetron source. During deposition, a  $-45$  V bias was applied to the sample with respect to the target. The critical temperature of the superconducting transition temperature of thin films with a layer thickness of 100 nm was measured to be 14.1 K in zero magnetic field.

For the shielded samples S1 and S2, quasiparticle traps were fabricated by first cleaning the Al surface by means of argon plasma milling at  $p = 0.2$  mTorr and *in-situ* evaporation of 25 nm Ti and 100 nm Au films at a base pressure of  $\sim 10^{-7}$  Torr (see Fig. S1c and d).

Care was taken to remove resist mask residues after each electron beam writing step using a remote oxygen plasma etch with a pressure of 1 mbar.

device	island size (nm $\times$ nm)	junction size (nm $\times$ nm)	NbTiN thickness (nm)	traps	oxygen exposure (Torr $\times$ s)	$R_N$ (k $\Omega$ )
N	500 $\times$ 500	200 $\times$ 200	70	no	7400	58
S1	450 $\times$ 200	200 $\times$ 200	100	yes	150	125
S2	450 $\times$ 250	200 $\times$ 250	100	yes	150	66

TABLE S1. Device fabrication parameters of the CPTs discussed in the main text.

### MEASUREMENT SETUP

The measurements were performed in a Leiden Cryogenics CF-1200 dry dilution refrigerator with a base temperature of 12 mK equipped with Cu/Ni shielded twisted pair cables thermally anchored at all stages of the refrigerator.

Fig. S2a shows the schematics of the measurement. The current bias and gate voltage were applied through battery operated and optically isolated sources in order to reduce line interference. Similarly, the first stage of the  $V_{\text{sd}}$  amplifier was isolated from the commercial readout electronics. Filtering of the measurement lines was achieved by room temperature LC  $\pi$  filters with a cutoff frequency of  $\sim 100$  MHz followed by a sequence of a high frequency copper powder filter [30] and a two-pole RC filter with a nominal  $f_{-3\text{dB}} = 50$  kHz, both thermally anchored to the 12 mK stage.

Special care was taken to avoid stray microwave radiation by using an outer and an inner copper shield enclosing the device. The inner surface of both shields was treated with commercially available Aeroglaze Z306 paint [31] absorbing far infrared stray radiation [32]. We note that the inner shield was not present for device N.

A typical DC  $V - I$  trace of device S2 at 12 mK temperature is presented in Fig. S2b exhibiting a sharp transition between the dissipationless and the resistive state at the switching current,  $I_{\text{sw}}$ . We observe a retrapping current  $I_r \ll I_{\text{sw}}$  characteristic to unshunted Josephson junctions in the low temperature limit [33]. The additional features in the resistive state are consistent with Fiske steps [34].

The switching current histograms were acquired using a Rigol DG4062 arbitrary waveform generator controlling the isolated current bias source with a triangle wave signal resulting in a  $dI/dt$  current ramp. A finite voltage response above the preset  $V_{\text{ref}} \sim 10 \mu\text{V}$  triggers the recording of  $I_{\text{sw}}$  (Fig. S2c). We note that the delay of the low pass filters were accounted for on the basis of circuit simulations. Subsequent  $I_{\text{sw}}$  measurements were taken with setting zero  $I_{\text{bias}}$

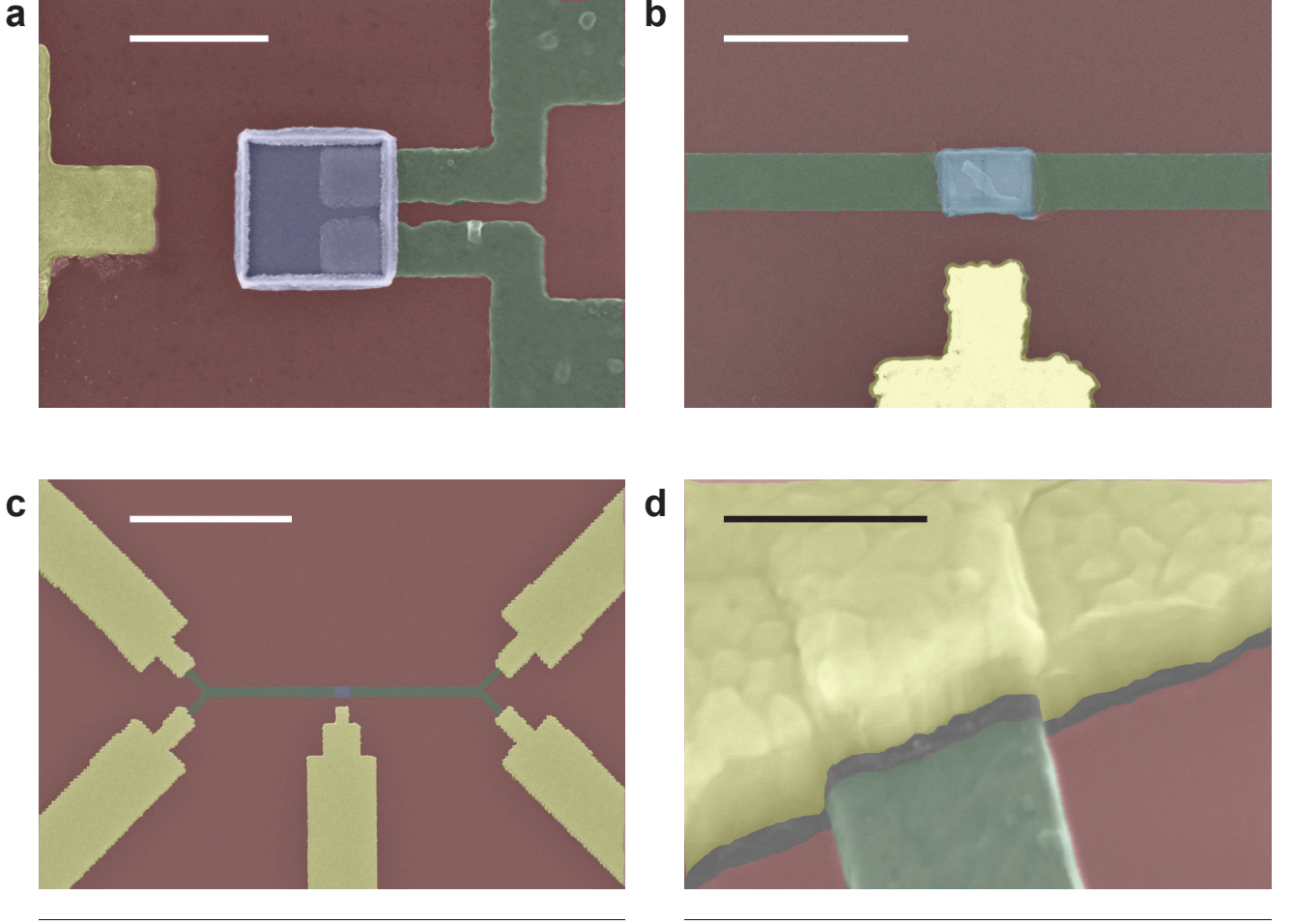


FIG. S1. **Scanning electron microscope images of the CPTs.** (a) Non-shielded device N without quasiparticle traps. (b), (c), (d) Shielded device S2 featuring quasiparticle traps. Colour legend: dark red: Si/SiO<sub>2</sub> substrate; light blue: NbTiN island, green: aluminium leads and yellow: normal metal (Ti/Au) gate and quasiparticle traps. Scale bars denote 500 nm (a), 1000 nm (b), 5  $\mu$ m (c) and 200 nm (d), respectively.

for approximately 100 ms in between to avoid overheating effects. We did not observe a difference in the switching current histograms taken with waiting times in the range of 20 ms and 10 s.

### BASIC CHARACTERIZATION OF THE CPT

In Fig. S3a we present a typical charge stability diagram of the CPT. First, we establish the superconducting gap of the aluminium lead and NbTiN island by finding the onset of quasiparticle transport (Fig. S3b and c).

device	$\Delta_{Al}$ ( $\mu$ eV)	$\Delta_{NbTiN}$ ( $\mu$ eV)	$R_N$ (k $\Omega$ )	$E_J$ ( $\mu$ eV)	$E_c$ ( $\mu$ eV)	$E_J/E_c$ calc.	$E_J/E_c$ $I_{sw}$
N	210	1390	58	54	50	1.08	1.25
S1	218	1420	125	21	62	0.34	0.32
S2	220	1300	66	48	49	0.98	1.16

TABLE S2. **Device transport parameters.**

It is important to note that we find a finite subgap conductance at  $eV_{sd} < 2\Delta_{NbTiN}$  which is consistent with the presence of the subgap quasiparticle states justifying the analysis leading to equation (1) in the main text.

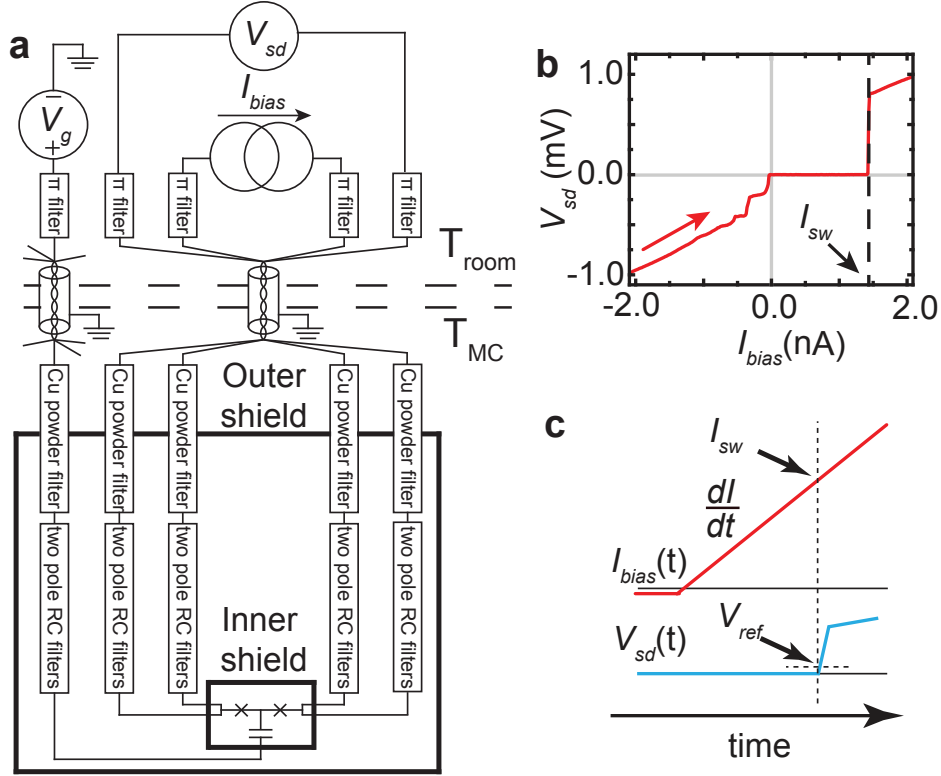


FIG. S2. **Measurement electronic setup and typical waveforms.** (a) Schematics of the measurement. (b) Typical experimental  $V - I$  trace exhibiting a well-defined switching current,  $I_{sw}$ . (c) Current ramp (red) with a slope of  $dI/dt$  probing  $I_{sw}$  which is recorded when the measured  $V_{sd}$  (blue) reaches  $V_{ref} \sim 10 \mu V$ .

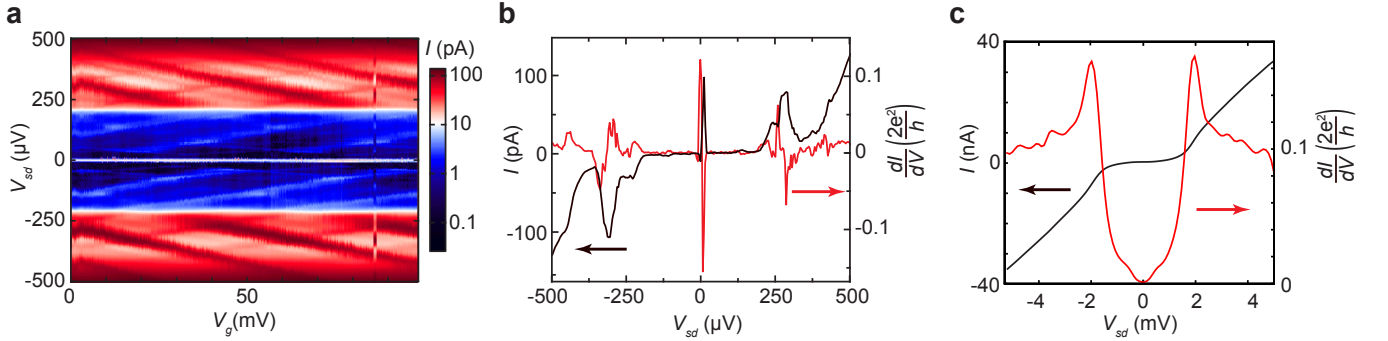


FIG. S3. **Basic characterization of the CPT.** (a) Stability diagram:  $\log |I|$  as a function of  $V_{sd}$  and  $V_g$ . We estimate  $E_c$  based on the characteristic resonances (see text). (b),(c)  $I - V$  (black) and  $dI/dV$  (red) line traces on the scale of  $\Delta_{Al}$  and  $\Delta_{NbTiN}$ , respectively. All data was taken for device S1.

Furthermore, we observe reduced  $\Delta_{NbTiN} \approx 1.3 \dots 1.4 \text{ meV}$  values compared to that of bulk films ( $\Delta > 2 \text{ meV}$ ) [35], which we attribute to the chemical interaction between the  $AlO_x$  tunnel barrier and the NbTiN film. Indeed, it was shown earlier that the critical temperature of Nb films is particularly very sensitive to contamination with oxygen [36, 37]. However, the nitridized NbTiN compound is presumably less prone to oxidation [38].

We evaluate the Josephson coupling for a *single* tunnel junction [39]:

$$E_J = \frac{\hbar}{2e^2} \frac{\Delta_{Al}}{R_N/2} K \left( \sqrt{1 - \left( \frac{\Delta_{Al}}{\Delta_{NbTiN}} \right)^2} \right) \quad (S1)$$

with  $K(x)$  being the complete elliptic integral of the first kind. This expression is valid in the zero temperature limit,



assuming symmetric tunnel junctions of the resistance of  $R_N/2$ .

We estimate the charging energy,  $E_c = e^2/2C$ , based on the periodicity of characteristic resonances visible for  $eV_{sd} \leq 2\Delta_{Al}$  (Fig. S3a) [40, 41].

Alternatively, we can estimate the  $E_J/E_c$  ratio based on the modulation of  $I_{sw}$  as a function of the gate charge,  $n_g$  (last column of Table S2) [42]. We find a good agreement between the  $E_J/E_c$  values acquired by the two independent methods.

#### EVALUATION OF THE PARITY LIFETIME

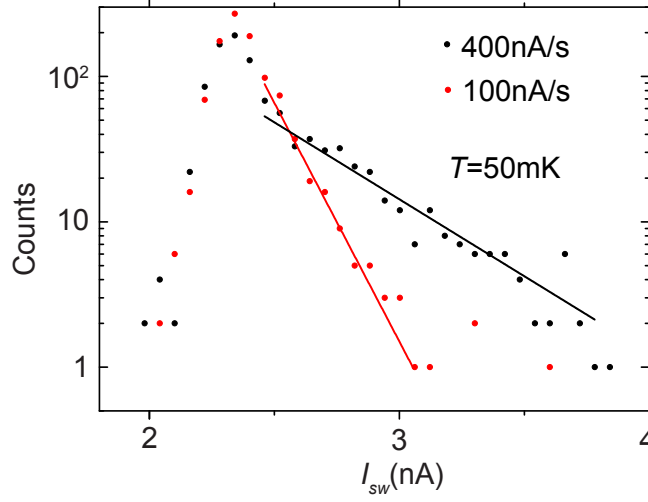


FIG. S4. **Measured switching current histograms at different  $dI/dt$  ramp rates.** Colour legend: red:  $dI/dt = 100$  nA/s, black:  $dI/dt = 400$  nA/s. The data was acquired on a CPT similar to device N.

We checked the robustness of the extracted parity lifetime against changing the current ramp rate. Typical datasets are shown in Fig. S4, giving  $\tau_p = 1.2$  ms and  $\tau_p = 0.98$  ms for  $dI/dt = 100$  nA/s (red) and  $dI/dt = 400$  nA/s (black), respectively. We estimate the typical uncertainty to be 15%, concluding that  $\tau_p$  does not depend on  $dI/dt$  which validates the analysis in the main text. However, we do not discuss here the intrinsic peak shapes of the bimodal switching current histogram. Since fast gate charge noise influences the measured distribution [43], we cannot distinguish between thermally activated [44] and macroscopic quantum tunneling behaviour [33, 45].

We now turn to the temperature dependence of  $\tau_p$ . In order to get equation (1) in the main text, we assume the following:

- i) The superconducting gap of the island ( $\Delta_{NbTiN} \gtrsim 1.3$  meV) is much higher than the effective thermal energy describing the quasiparticle population and the gap of the leads ( $\Delta_{Al} \approx 200$   $\mu$ eV).
- ii) The density of states in the leads is BCS-type:  $\rho_{lead}(E) = \rho_{Al} \times |E|/\sqrt{E^2 - \Delta_{Al}^2}$  for  $|E| > \Delta_{Al}$  and zero otherwise.
- iii) There is a constant, finite subgap density of states  $\rho_{subgap}$  for energies below  $\Delta_{NbTiN}$  in the island.
- iv) the energy dependence of the single electron tunnel probability is negligible over the energy range of  $\sim \Delta_{NbTiN}$ , meaning that the tunnel barrier is much higher than  $\Delta_{NbTiN}$ .
- v) The tunnel barriers are identical, each characterized by half the normal state resistance of the full device,  $R_N$ .

Considering only single electron tunneling and zero voltage bias across the tunnel barriers, following [46], we get the quasiparticle tunnel rate:

$$\tau_p^{-1} = \frac{2}{e^2(R_N/2)\rho_{Al}} \frac{\rho_{subgap}}{\rho_{NbTiN}} \int_0^\infty \rho_{lead}(E) f(T, E) dE = \frac{2n_{qp}}{e^2 R_N \rho_{Al}} \frac{\rho_{subgap}}{\rho_{NbTiN}}. \quad (S2)$$

Assigning an effective temperature to the quasiparticle population in the leads, we find:

$$n_{\text{qp}}(T) = 2 \int_0^\infty \rho_{\text{lead}}(E) f(T, E) dE = \rho_{\text{Al}} \sqrt{2\pi k_B T \Delta_{\text{Al}}} e^{-\frac{\Delta_{\text{Al}}}{k_B T}} \quad (\text{S3})$$

in the limit of  $k_B T \ll \Delta_{\text{Al}}$ . For temperatures exceeding 100 mK, we assume that the quasiparticle population is in thermal equilibrium, and therefore the lattice temperature is equivalent to the effective quasiparticle temperature:  $\tau_p^{-1}(T) \propto \sqrt{T} \exp(-\Delta_{\text{Al}}/k_B T)$ .

We verify this picture by fitting the observed parity lifetimes with  $\Delta_{\text{Al}}$  as a free parameter, and find values ranging 170...210  $\mu\text{eV}$  for different devices in good correspondence with the gap determined by voltage bias spectroscopy ( $\Delta_{\text{Al}}$  in Table S2).

Notably, the ratio  $\rho_{\text{subgap}}/\rho_{\text{NbTiN}}$  is the Dynes parameter [47] of the island material, characterized to be  $\lesssim 10^{-3}$  based on measurements of highly resistive single junctions. With this value and using  $\rho_{\text{Al}} = 1.45 \times 10^{47} \text{ J}^{-1} \text{ m}^{-3}$  [46], we get  $n_{\text{qp}} \sim 3 \mu\text{m}^{-3}$  for device N based on the observed parity lifetime of 9.5 ms in the low temperature limit.

We now comment on the observed  $\Delta^* \approx 20 \mu\text{eV}$  activation energy observed for devices S1 and S2. We estimate the maximal even-odd energy difference to be  $\delta E \approx 20 \dots 30 \mu\text{eV}$  based on  $E_J \approx E_c \approx 50 \mu\text{eV}$  [48] which is in range of the experimentally observed  $\Delta^*$ . Similar, activated behaviour of the parity lifetime scaling as  $\sim \exp(\delta E/k_B T)$  was reported earlier [49].

Providing another possible explanation, we note that a grain size of  $\approx 50 \text{ nm}$  can lead to a level spacing of the order of  $10 \mu\text{eV}$  which can influence single electron transport and hence  $\tau_p$  if the grains are weakly coupled, i. e. for disordered superconducting films [50]. Disorder-induced fluctuations may also explain the broadening of the coherence peaks (Fig. S3c) [51, 52].

## SUPERCONDUCTING THIN FILM CHARACTERIZATION AND MAGNETIC FIELD DEPENDENCE

Next, we consider the properties of superconducting stripes with layer thickness  $d$ , and a width  $w$  to find the London penetration depth  $\lambda_L$  and the coherence length  $\xi$ . We characterize the upper critical field in the parallel ( $B_{c\parallel}$ ) and perpendicular geometry ( $B_{c\perp}$ ) based on the  $dI/dV$  traces of the tunnel junctions of the CPT. In addition, we measure the normal state resistivity of the films that gives an estimate for the mean free path,  $l_m$  [53].

First, we establish the length scales of the island material, NbTiN. We find films superconducting at  $B_\perp = 9 \text{ T}$  which leads to an upper limit of  $\xi_{\text{NbTiN}} < 6 \text{ nm}$  following [54]:

$$B_{c\perp} = \frac{\Phi_0}{2\pi\xi^2}. \quad (\text{S4})$$

The penetration depth can be estimated using the normal state resistivity of  $\rho = 98 \mu\Omega\text{cm}$  and the critical temperature of  $T = 14.1 \text{ K}$  using the following semi-empirical formula [35]:

$$\lambda_{\text{NbTiN}} = \sqrt{\frac{\rho[\mu\Omega\text{cm}]}{T_c[\text{K}]}} \times 105 \text{ nm} \approx 280 \text{ nm}. \quad (\text{S5})$$

Next we estimate length scales of the Al leads based on the electronic transport through the CPT. Typical thin Al films are type-II superconductors in the dirty limit ( $l_m < \xi_0$ ) with a reduced coherence length of  $\xi \approx 0.85\sqrt{\xi_0 l_m}$  and with a London penetration depth of  $\lambda \approx \lambda_0\sqrt{\xi_0/l_m}$ , where  $\xi_0 \approx 1500 \text{ nm}$  and  $\lambda_0 \approx 16 \text{ nm}$  are the bulk values [54]. For our films, we estimate  $l_m \approx 8.5 \text{ nm}$  based on the resistivity of  $\rho = 4.3 \mu\Omega\text{cm}$  [53]. From the stability diagram of the devices, we extract upper critical fields of  $B_{c2,\perp} = 36.4 \pm 4 \text{ mT}$  (Fig. S5d) and  $B_{c2,\parallel} = 320 \pm 10 \text{ mT}$  (Fig. S5b) leading to a coherence length of  $\xi_{\text{Al}} = 96 \text{ nm}$  and  $\lambda_{\text{Al}} = 230 \text{ nm}$  which enables vortex formation in the aluminium leads in perpendicular magnetic field.

It is important to observe that  $\xi_{\text{NbTiN}} \ll d \approx 100 \text{ nm}$  enables vortex formation for an *in-plane* geometry in the NbTiN island. We find a characteristic suppression of  $\tau_p$  at  $B_\parallel = 70 \text{ mT}$  for device S2 (orange dots in Fig. S5a) and at  $B_\parallel = 110 \text{ mT}$  for device S1 (cyan dots in Fig. S5a). Considering the effective cross-sectional areas (see Table S1 for dimensions), we find  $\Phi \approx 1.5\Phi_0$  and  $\Phi \approx 1.1\Phi_0$  for S2 and S1, respectively, which is in qualitative agreement with the threshold of a single vortex formation in a mesoscopic island [55–57]. We also note that  $B_{c2,\parallel}$  of the leads (Fig. S5b) does not depend on the direction of  $B_\parallel$ , therefore the different evolution of  $\tau_p$  can only be explained by the different alignment of  $B_\parallel$  with respect to the NbTiN islands.

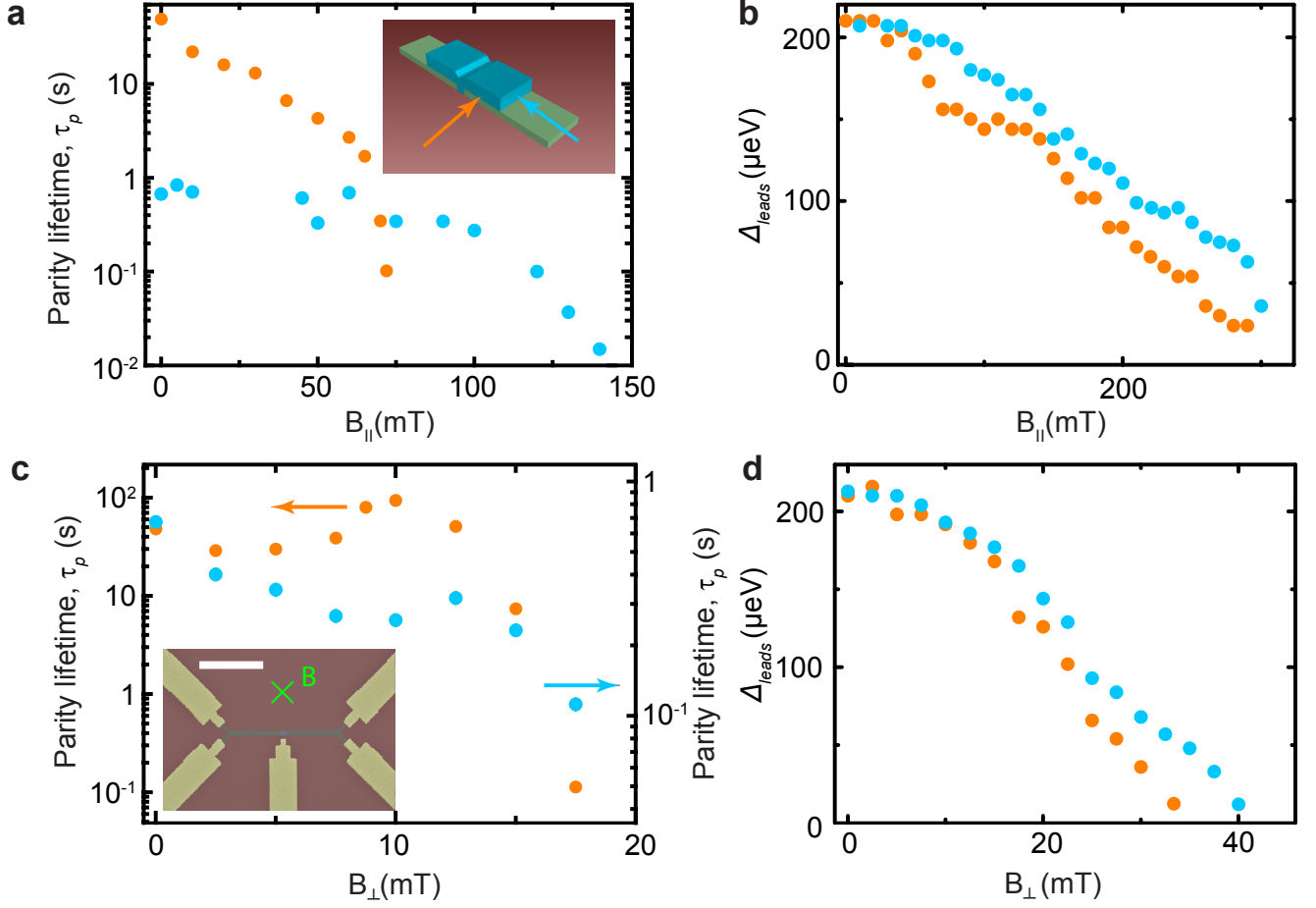


FIG. S5. **Parity lifetime and superconducting gap in magnetic field.** (a) Measured parity lifetime as a function of in-plane magnetic field. The inset shows the relative orientation of the field for the two devices. (b) The superconducting gap of the Al leads as a function of in-plane magnetic field. (c),(d) The parity lifetime and the superconducting gap as a function of the perpendicular magnetic field. Colour legend: cyan: device S1; orange: device S2. The scale bar in the inset of panel (c) denotes  $5 \mu\text{m}$ .

In a perpendicular geometry, the vortex phase is stable in a thin stripe above the magnetic field

$$B_{c1,\perp}(w) = \alpha \frac{\Phi_0}{w^2}, \quad (\text{S6})$$

where  $\alpha$  is a model-dependent prefactor [58–60] of the order of unity. We reproducibly find the same non-monotonic behaviour of  $\tau_p$  for devices S1 and S2 with the maximum at  $B_{\perp} \approx 10 \dots 13 \text{ mT}$ , which is in range of  $B_{c1,\perp}(w)$  for  $w = 200 \dots 250 \text{ nm}$ , the width of the Al leads near the island.

- 
- [30] F. Mueller, R. N. Schouten, M. Brauns, T. Gang, W. H. Lim, N. S. Lai, A. S. Dzurak, W. G. van der Wiel, and F. A. Zwanenburg, *Review of Scientific Instruments* **84**, 044706 (2013).
  - [31] <http://www.lord.com/products-and-solutions/coatings/aeroglaze-z306-polyurethane-coating>.
  - [32] M. J. Persky, *Review of Scientific Instruments* **70**, 2193 (1999).
  - [33] D. Massarotti, L. Longobardi, L. Galletti, D. Stornaiuolo, D. Montemurro, G. Pepe, G. Rotoli, A. Barone, and F. Tafuri, *Low Temperature Physics* **38**, 263 (2012).
  - [34] D. Coon and M. Fiske, *Phys. Rev.* **138**, A744 (1965).
  - [35] T. Matsunaga, H. Maezawa, and T. Noguchi, *Applied Superconductivity*, *IEEE Transactions on* **13**, 3284 (2003).
  - [36] C. Koch, J. Scarbrough, and D. Kroeger, *Phys. Rev. B* **9**, 888 (1974).
  - [37] J. Halbritter, *Applied Physics A* **43**, 1 (1987).

- [38] A. Darlinski and J. Halbritter, *Surface and Interface Analysis* **10**, 223 (1987).
- [39] V. Ambegaokar and A. Baratoff, *Phys. Rev. Lett.* **10**, 486 (1963).
- [40] D. B. Haviland, Y. Harada, P. Delsing, C. D. Chen, and T. Claeson, *Phys. Rev. Lett.* **73**, 1541 (1994).
- [41] J. J. Toppari, T. Kühn, A. P. Halvari, J. Kinnunen, M. Leskinen, and G. S. Paraoanu, *Phys. Rev. B* **76**, 172505 (2007).
- [42] K. A. Matveev, M. Gisselält, L. I. Glazman, M. Jonson, and R. I. Shekhter, *Phys. Rev. Lett.* **70**, 2940 (1993).
- [43] P. Joyez, *The single Cooper pair transistor: a macroscopic quantum system*, Ph.D. thesis, Universite Paris 6 (1995).
- [44] T. A. Fulton and L. N. Dunkleberger, *Phys. Rev. B* **9**, 4760 (1974).
- [45] J. Clarke and F. K. Wilhelm, *Nature* **453**, 1031 (2008).
- [46] O.-P. Saira, A. Kemppinen, V. F. Maisi, and J. P. Pekola, *Phys. Rev. B* **85**, 012504 (2012).
- [47] R. Dynes, V. Narayanamurti, and J. Garno, *Phys. Rev. Lett.* **41**, 1509 (1978).
- [48] R. M. Lutchyn, *Phys. Rev. B* **75**, 212501 (2007).
- [49] N. A. Court, A. J. Ferguson, R. Lutchyn, and R. G. Clark, *Phys. Rev. B* **77**, 100501 (2008).
- [50] Y. Dubi, Y. Meir, and Y. Avishai, *Nature* **449**, 876 (2007).
- [51] B. Sacepe, T. Dubouchet, C. Chapelier, M. Sanquer, M. Ovadia, D. Shahar, M. Feigel'man, and L. Ioffe, *Nat Phys* **7**, 239 (2011).
- [52] P. C. J. J. Coumou, E. F. C. Driessen, J. Bueno, C. Chapelier, and T. M. Klapwijk, *Phys. Rev. B* **88**, 180505 (2013).
- [53] C. Kittel, *Introduction to solid state physics*, 5th ed. (New York: Wiley, 1976).
- [54] M. Tinkham, *Introduction to Superconductivity*, edited by D. Publications (Dover Publications, 2004).
- [55] V. V. Moshchalkov, L. Gielen, C. Strunk, R. Jonckheere, X. Qiu, C. V. Haesendonck, and Y. Bruynseraede, *Nature* **373**, 319 (1995).
- [56] A. K. Geim, I. V. Grigorieva, S. V. Dubonos, J. G. S. Lok, J. C. Maan, A. E. Filippov, and F. M. Peeters, *Nature* **390**, 259 (1997).
- [57] J. J. Palacios, *Phys. Rev. B* **58**, R5948 (1998).
- [58] G. Stan, S. B. Field, and J. M. Martinis, *Phys. Rev. Lett.* **92**, 097003 (2004).
- [59] J. T. Peltonen, J. T. Muhonen, M. Meschke, N. B. Kopnin, and J. P. Pekola, *Phys. Rev. B* **84**, 220502 (2011).
- [60] I. Aranson, M. Gitterman, and B. Y. Shapiro, *Phys. Rev. B* **51**, 3092 (1995)